MARS
The International Journal of Mars Science and Exploration

MARS INFORMATICS
Open Access Journals

Technology

Calibration and Performance of the Mars Reconnaissance Orbiter Context Camera (CTX)

James F. Bell III[1], Michael C. Malin[2], Michael A. Caplinger[2], Joseph Fahle[2], Michael J. Wolff[3], Bruce A. Cantor[2], Philip B. James[3], Tony Ghaemi[2], Liliya V. Posiolova[2], Michael A. Ravine[2], Kimberley D. Supulver[2], Wendy M. Calvin[4], R. Todd Clancy[3], Kenneth S. Edgett[2], Laurence J. Edwards[5], Robert M. Haberle[5], Amy Hale[6], Steven W. Lee[7], Melissa S. Rice[8], Peter C. Thomas[8], and Rebecca M.E. Williams[9]

[1]School of Earth & Space Exploration, Arizona State University, Tempe, AZ, 85287, USA, Jim.Bell@asu.edu; [2]Malin Space Science Systems, Inc., San Diego, CA, 92191, USA; [3]Space Science Institute, Boulder, CO, 80303, USA; [4]Dept. of Geological Sciences, University of Nevada, Reno, NV, 89557, USA; [5]NASA/Ames Research Center, Moffett Field, CA, 94035, USA; [6]Jet Propulsion Laboratory/California Institute of Technology, Pasadena, CA, 91109, USA; [7]Denver Museum of Nature and Science, Denver, CO, 80205, USA; [8]Dept. of Astronomy, Cornell University, Ithaca, New York, 14853, USA; [9]Planetary Science Institute, Tucson, AZ, 85719, USA.

Citation: MARS 8, 1-14, 2013; doi:10.1555/mars.2013.0001
Submitted: December 10, 2011; Revised March 28, 2012; Accepted: April 15, 2013 ; Published: April 15, 2013
Editor: David A. Paige, Dept. of Earth, Planetary and Space Sciences, University of California, Los Angeles
Reviewers: Jeffrey R. Johnson, Johns Hopkins University Applied Physics Laboratory; W. Alan Delamere, Delamere support systems

Abstract

Background: The Context Camera (CTX) instrument aboard the NASA Mars Reconnaissance Orbiter (MRO) spacecraft is a 5056-pixel CCD line-scan imager that uses pushbroom scanning along the direction of spacecraft motion to acquire ~30 km wide image strips at a spatial resolution of ~6 m/pixel from MRO's nominal circular polar orbit. We describe here the pre-flight and in-flight measurement, test, and validation activities and calibration pipeline algorithms that enable raw CTX data to be converted to absolute radiance on sensor, radiance factor, or estimated Lambert albedo.

Results: The CTX CCD has a gain of 72.6±3.1 e^-/DN, a read noise of 66.0±2.5 e^-, a full well of 267,000±10,000 e^-, and a highly linear response. CCD bias levels are typically < 2% of the full 12-bit range, and dark current is negligible at typical operating temperatures at Mars. Raw images exhibit flatfield variations of approximately ±20%, varying by less than ±1% during operations at Mars. The CTX spectral response profile has an effective band center of 611±189 nm. A correction for small geometric distortion has been derived. The CTX radiometric response coefficient is ~ 13.1 (DN/msec)/(W/m^2/micron/sr), with an estimated qualitative uncertainty of 10-20% based on comparisons of derived albedos of the same regions from different missions. In-flight tests reveal scattered light levels to be < 1% and stray light to be < 3-5% of on-axis signal levels. Overall, CTX performance has been stable over the course of the MRO Primary Science Phase and Extended Missions. As of early-2013, the instrument has mapped ~80% of Mars at a scale of ~6 m/pixel.

Introduction

The Context Camera (CTX) is one of the primary science payload instruments on the NASA Mars Reconnaissance Orbiter (MRO) mission (Zurek and Smrekar, 2007). CTX has been acquiring high-resolution monochromatic images of Mars since 2006, and has now imaged most of the planet at a scale of 6 m/pixel. CTX data are being widely used in the Mars community for a variety of focused photogeologic studies, as well as in base maps and regional geologic context mosaics for use with other Mars orbital data sets in many other surface science and landing site selection studies.

A detailed understanding of the performance and calibration of the CTX could provide additional insights and information for colleagues who are creating or working with CTX images and mosaics, especially if quantitative information needs to be derived from the measurements

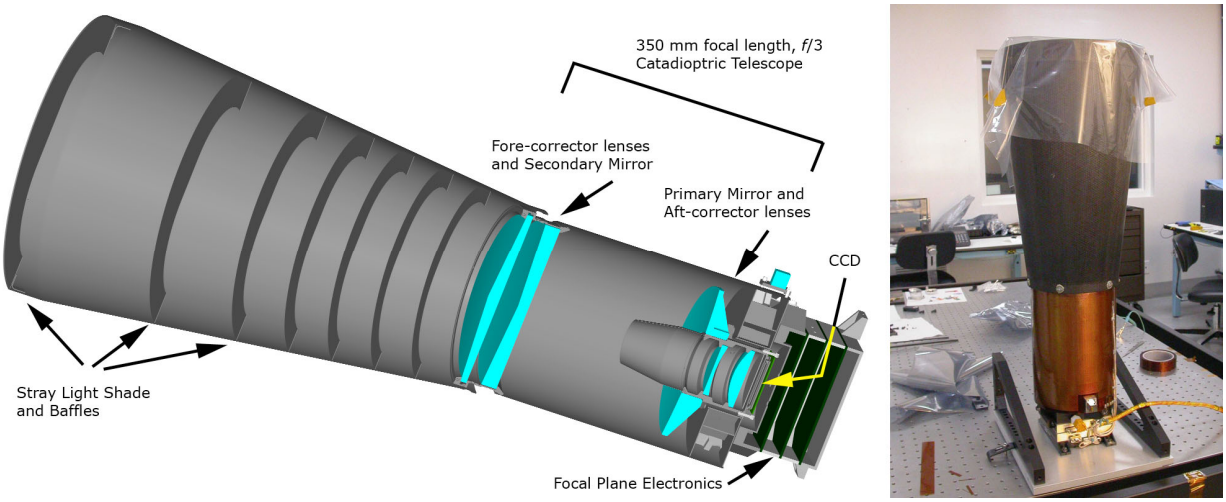

Figure 1. (Left) Design representation of the MRO CTX catadioptric telescope and focal plane array assembly. (Right) Assembled CTX camera on the optical bench at MSSS. The primary mirror is ≈ 108 mm in diameter (Figure01.jpg).

(*e.g.,* photogrammetry, albedo). Thus, our goal here is to describe the CTX instrument, its requirements, its operations, and its calibration methodology in sufficient detail to allow the potential uses and limitations of the CTX data set to be well understood. This paper should be considered as a companion to that of Malin et al. (2007), which provides additional details on the design and operation of the instrument and the scientific goals of the CTX investigation.

CTX uses a 350 mm focal length catadioptric telescope (Fig. 1; Malin et al. 2007) with a focal ratio of *f*/3.05 on-axis, and *f*/3.13 at the edge of the 5.7° field of view. While imaging Mars from MRO's ~300 km altitude circular, polar orbit, the CTX ground track moves from south to north on the planet's dayside. The detector is a Kodak KLI-5001G 5056-pixel linear CCD (38 masked reference pixels, then 5000 active 7×7 µm pixels, then 18 more masked reference pixels), with output data digitized to 12 bits (0-4095 Data Numbers or DNs). The CTX pixels are divided electronically into an A channel and a B channel, alternating by pixel. Each pixel's instantaneous field of view of ~20 mrad yields a spatial resolution of ~6 m/pixel over a ~30 km image width. Long (many hundreds of km) swaths of the surface are imaged by orienting the line array perpendicular to the direction of spacecraft motion and "pushbrooming" along the direction of spacecraft motion. Images can be compressed using both lossy and lossless methods. Optionally, the data can also be summed 2×2 to reduce data volume (at the expense of degraded resolution). CTX was designed, fabricated, and tested by Malin Space Science Systems, Inc. (San Diego, CA) in 2004 and 2005. It was launched on MRO on 12 August 2005, and has been operating successfully in Martian orbit since March 2006. As of late April, 2013, the instrument had acquired images of 82.2% of the Martian surface at a resolution of ~6 m/pixel, with 34.6% covered more than once for stereo, change monitoring, or clearer-atmosphere repeat imaging.

Achieving the goals of the CTX investigation (Malin et al. 2007) requires accurate initial calibration and testing of the camera system (optics plus detector and electronics) and further validation and monitoring of the calibration and performance in-flight during nominal operations at Mars. Additional science investigations using CTX data, such as assessment of quantitative surface albedo variations or radiative transfer modeling of the Martian surface and atmosphere could also require the creation of accurate absolute calibration of CTX images. Here we describe the pre-flight and in-flight tests, the measurements, and the models that enable the calibration of CTX images; document the instrument's performance and estimated calibration accuracy during nominal MRO operations; and describe the format and content of raw CTX images and calibration files that are archived in the NASA Planetary Data System (PDS).

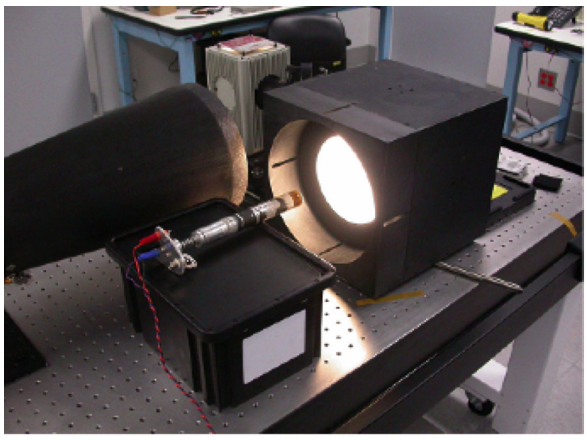

Figure 2. Setup used in MSSS optical bench and diffuse integrating sphere (bright source within the black box on the right) testing of the CTX instrument. A calibrated photodiode (foreground silver cylinder) and the CTX telescope (black conical cylinder in background) were alternately pointed into the sphere's exit port (Figure02.jpg).

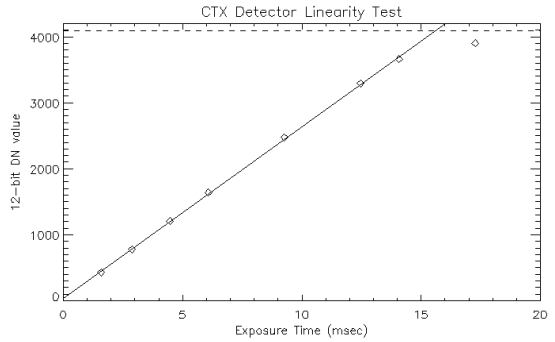

Figure 3. CTX flight detector linearity test data acquired on 11 October 2004, using the test setup shown in Figure 2. The solid line is a linear fit to all of the data except the longest exposure time data point. The data show a linear correlation coefficient > 0.9998 for 12-bit DN values up to about 3600 DN. The statistical error bars on each of the data points are comparable to the height of each symbol (Figure03.jpg).

CTX pre-flight calibration: Methods and results

Pre-flight testing of CTX was designed to characterize or verify many of the basic properties of the CCD detector, as well as to measure or estimate the instrument's system spectral throughput, geometric distortion, and radiometric responsivity. Additional tests were performed to characterize the level of off-axis stray or scattered light in the detector's field of view, which was found to be less than 0.6% of the on-axis signal (Malin et al. 2007). Here we briefly report on the results and highlights of this pre-flight calibration exercise. Detailed descriptions of the tests and methods may be found in the MRO MARCI and CTX Pre-Flight Calibration Report (MRO, 2005).

CCD characterization: Linearity, gain, full well, read noise

The CTX was configured on an optical bench to stare into the exit port of a diffuse integrating sphere that was illuminated by a Quartz-Halogen lamp (Fig. 2). The radiant output of the lamp was characterized using a NIST-certified photodiode.

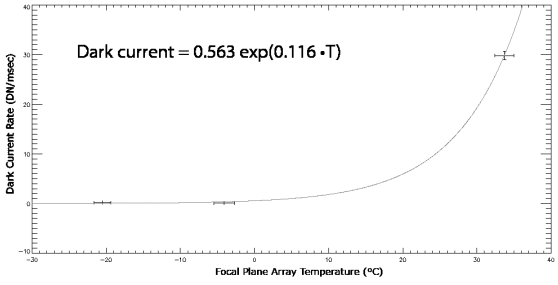

Figure 4. CTX dark current data (points) and exponential model (line) of dark current rate (DN/msec) vs. average focal plane array temp. (°C). (Figure04.jpg).

To assess the linearity of the CTX detector, we acquired a series of images of the sphere exit port using an increasing exposure time until detector saturation was reached. An analysis of the data (Fig. 3) reveals that the CTX detector responds linearly (Pearson correlation coefficient > 0.9998) over a range of 12-bit DN values up to about 3600 DN, or about 88% of the maximum dynamic range. It should be noted that this can be considered to be nominal performance for a modern CCD detector. From the perspective of operational limitations, CTX exposure times in flight are generally set by an automated onboard calibration process (performed after every CTX power cycle and prior to each targeted image acquisition) to keep predicted signal levels from exceeding ~2000-2500 DN.

A similar image sequence was obtained to characterize the gain, read noise, and full well values of the CTX detector using the photon transfer technique (also known as "light transfer curves" or "signal vs. noise plots"; Janesick et al. 1987; Bell et al. 2009). Overall, nineteen CTX image data sets with good signal levels and supporting dark frames (which contained no evidence of drift) were used for photon transfer processing. Analysis of this data set produces a mean scale factor to convert between DN and electrons (the gain) of 72.6 ± 3.1e^-/DN, and an average zero-exposure noise (read noise) value of 66.0 ± 2.5 e^-. Multiplying the average gain value by the approximate DN level at which the linearity data begin to exhibit signs of saturation (Fig. 3) results in an estimate of the full-well of the CTX CCD of 267,000 ± 10,000 e^-. This uncertainty on the full-well level is considered conservative and driven primarily by the difficulty of determining the saturation level from the sparsely sampled test to a precision better than a few hundred 12-bit DN values. Table 1 summarizes the CCD parameters derived from these tests.

Table 1. MRO CTX Instrumental Parameters

Parameter	***Value (± 1σ)***	***Units***
CCD		
Linearity	> 0.9998	Pearson correl. coefficient
Gain	72.6 ± 3.1	electrons/DN
Read Noise	66.0 ± 2.5	electrons
Full Well	267,000 ± 10,000	electrons
Spectral Passband		
Effective Wavelength	611	nm
FWHM of Passband	189	nm
Radiometry		
Calibration Coefficient	13.1	(DN/msec) / (W/m^2/μm/sr)
Uncertainty	10-20%	

Bias and dark current

The bias or un-illuminated background DN level of the CTX detector was monitored during pre-flight testing by analyzing the signal levels in the fully masked pixels on each end of the CTX 5056 pixel linear CCD array (pixels 1-38 and 5039-5056). During pre-flight testing the bias signal of the CTX array was always small (typically less than about 2% of the full 12-bit signal level), even at room temperature. However,

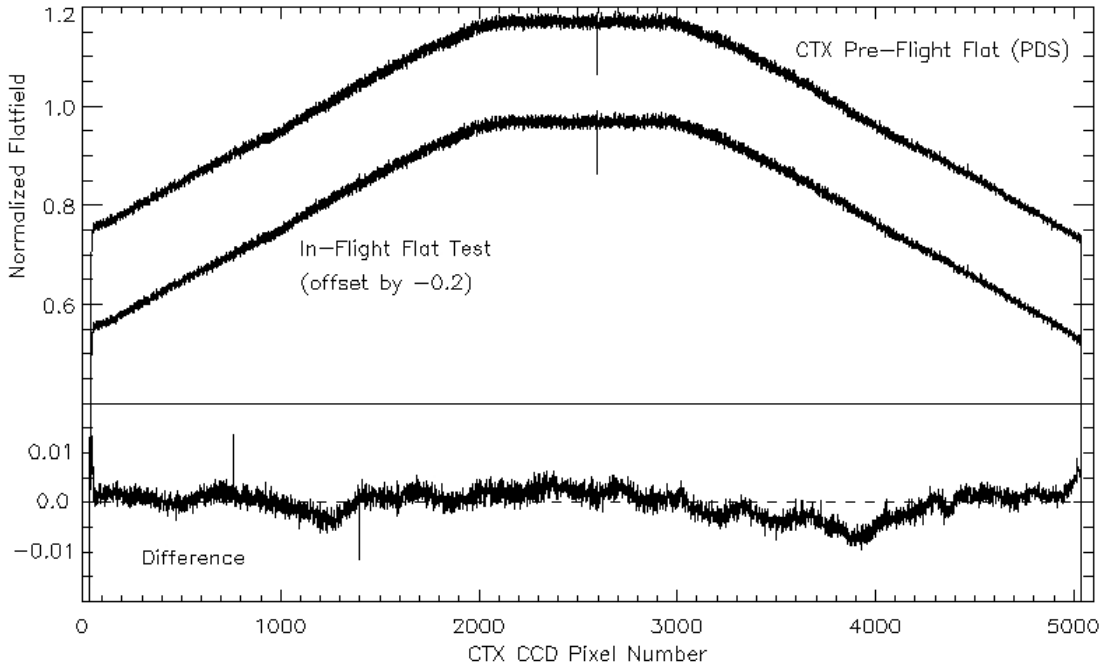

Figure 5. CTX pre-flight derived flatfield vector (top data) compared to data from an in-flight flatfield validation test (middle data). The bottom plot shows the difference (Figure05.jpg).

differences between the pre-flight ground support equipment electronics and the actual MRO flight electronics prevented the development of a precise in-flight bias model based on pre-flight testing data.

Regardless, a reasonable approximation of the CTX array's dark current behavior (thermally-generated signal) as a function of temperature could be made during the pre-flight testing by measuring a differential signal between the bias level at zero exposure time and the "dark signal" accumulated during nominal exposure times. Such CTX dark current images were acquired during two sets of pre-flight Thermal Vacuum (TV) tests and subsequently used to produce a model of the CTX dark current. The specific procedure consisted of six steps: (1) Estimating the CTX Focal Plane Array (FPA) temperatures for TV images using concurrent temperature measurements acquired from sensors mounted close to the FPA; (2) Identifying an appropriate subset of TV images at different temperatures to use for dark current modeling; (3) Calculating the average DN values for this subset of images; (4) Subtracting the bias from the calculated average DN using the average data of the masked-off reference pixels; (5) Generating a linear fit of dark current rate (DN/msec) versus exposure time at each temperature; and (6) Generating an exponential model of the dark current based on the derived dark current rate versus temperature.

For each pre-flight dark current data set in Fig. 4, the derived CTX dark current rates are plotted against the respective average FPA temperature. The resulting model of the CTX dark current is:

$$D_{\mathrm{CTX}} = 0.563e^{0.116T} \quad (1),$$

where D_{CTX} is the dark current accumulation rate in DN/msec and T is the recorded FPA temperature in degrees Celsius. This model predicts that the dark current is essentially zero at typical CTX flight operating temperatures (between about 17°C and 25°C, depending upon solar distance and orbital geometry; See Section 3.1). Subtraction of the average DN value of the masked reference pixels downlinked with each CTX image should thus remove almost all additional non-scene DN offset contributions from nominal CTX images at Mars. For verification and validation, reference pixel levels have been monitored during flight, and a limited set of dedicated bias and dark current observations have been acquired during cruise and Mars orbital operations (see Section 3.1).

Flatfield

For the purpose of constructing a flatfield (an assessment of pixel-to-pixel responsivity variations), CTX was mounted on a rotation stage and viewed the output port of the same integrating sphere as was used for the linearity and radiometry measurements (Fig. 2). The rotation stage allowed each part of the 5.7° CTX field of view to be scanned across the brightest and most uniform central region of the integrating sphere output port. The acquired image sequence started at +10° off the CTX optical axis and moved to -11° using an angular step of 0.5°.

A 1-dimensional flatfield array was created for each angular position by subtracting the dark reference pixels from each line of data and summing all (128) lines of data to improve

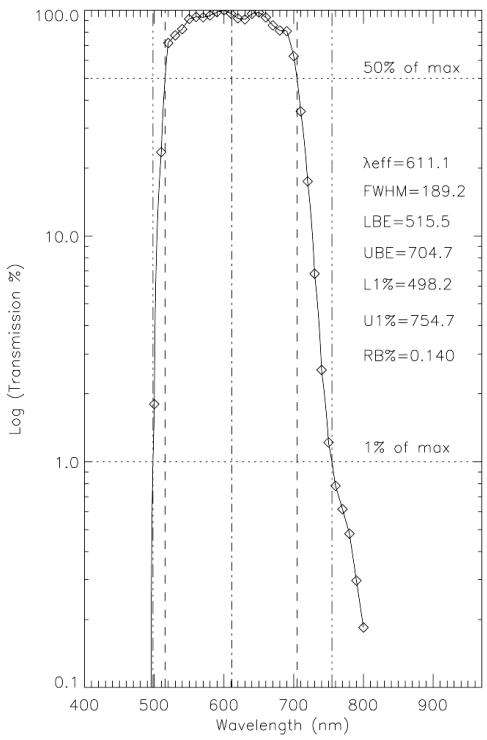

Figure 6. CTX system spectral throughput and derived passband parameters for effective wavelength (λ_{eff}), full-width at half max (FWHM), upper and lower 50% band edges (UBE, LBE), upper and lower 1% band edges (U1%, L1%), and rejection band (RB%) (Figure06.jpg).

the signal-to-noise ratio. The data from all positions were then combined into a new 5056-pixel flatfield array by choosing the maximum value for each pixel in the array. Finally, the entire new flatfield array was normalized to produce an average value of 1.0 (excluding the masked reference pixels) (see Fig. 5). As will be discussed in Section 3.2, an inflight check on the flatfield was made possible by special spacecraft maneuvers.

Spectral throughput

The CTX instrument's filter spectral throughput profile was published by Malin et al. (2007) (their Fig. 14) based on vendor measurements. The full CTX system (filter + optics + detector QE) spectral response was assessed using a monochromator. A series of images of the monochromator exit port were obtained for wavelength settings between 400 nm and 800 nm with steps of 10 nm. The experimental setup did not allow for the knowledge of the absolute radiance at the CTX aperture for each monochromator setting, and as such, the derived throughput is only a relative measure of the system responsivity. Nonetheless, the data (Fig. 6) are adequate to estimate the camera's effective band center (611 nm) and FWHM (189 nm).

No measurements characterizing the polarization of the CTX instrument were performed. This was motivated, in part, by the insignificant degree of polarization expected by scattering processes in the visible as viewed by CTX during normal operations. In addition, past experience indicates that the CTX flatfield correction will remove effectively any polarization effects introduced by the optical system itself.

Radiometry

Pre-flight calibration efforts included an attempt to estimate the CTX radiometric response using the same integrating sphere setup as employed for the flatfield measurements. However, errors in the determination of the absolute sphere radiance values (possibly due to an insufficient calibration of the photodiode) precluded our use of those data for radiometric calibration. Instead, we produced an estimate of the CTX radiometric response from a model used during pre-flight design and planning. This estimate was subsequently validated in-flight using comparisons of derived Lambert albedos for several areas on Mars as observed by CTX, MOC, MARCI, and MER/Pancam.

The "first principles" estimate of the CTX radiometric response coefficient employed a model developed from component-level and vendor test data for the quantum efficiency of the detector, the transmissivity of the filters and optics, the f-number of the optics, the CCD pixel size, and the electronics gain. Specifically, applying the vendor and component test data at 600 nm (near the center of the CTX bandpass) to the system spectral throughput results, the model predicts that a perfectly reflecting Lambert surface viewed at normal incidence and at Mars perihelion distance (1.38 AU) would generate approximately 266,000 e^-/msec within a CTX pixel, or a signal level of approximately 3660 DN/msec using the derived gain of the CTX CCD of 72.6 e^-/DN. Assuming a solar input radiance (Wehrli, 1986) at 1.38 AU as integrated over the CTX bandpass of 279 W/m^2/micron/sr, one arrives at an estimate of the CTX radiometric calibration coefficient of 13.1 (DN/msec)/(W/m^2/micron/sr).

Some of the input variables for this exercise are only estimates or approximations themselves. Accordingly, an analysis of the uncertainties in these variables indicates that the estimated radiometric coefficient may possess an uncertainty of the order 20%. Nonetheless, this process served as a good starting point for pre-flight exposure time planning, and subsequently from which in-flight validation experiments could be designed. As described below, the estimated coefficient value of 13.1 (DN/msec)/(W/m^2/micron/sr) was ultimately found to be within the ~10% (root-mean-square) scatter of Mars albedo measurements made for the same areas by other spacecraft investigations. As a result, in the absence of additional calibration opportunities, we have adopted our "first principles" estimate as the de-facto CTX radiometric calibration coefficient.

Geometric distortion

Geometric calibration of the CTX was performed using an autocollimator that projected a single vertical line onto the CTX focal plane and could rotate that line in 1° steps through the CTX field of view. The measured position of

Table 2. In-Flight CTX Dark Current Measurements.

File Name	Date (YYMMDD)	Exp (msec)	FPA Temp (°C)	Avg. 12-bit Dark Signal (DN ± 1σ)
P06_003416_3351_XN_24N123W	070419	1.87	20.2	8.1 ± 0.6
P12_005764_3494_XN_10N148W	071019	1.87	23.0	13.9 ± 0.6
P18_008118_0314_XN_31S321W	080420	1.87	19.8	12.6 ± 0.8
B02_010456_0246_XN_24S076W	081019	1.87	21.3	16.9 ± 0.9
B04_011261_3562_XN_03N118W	081221	1.87	20.8	4.8 ± 0.4
B08_012791_3567_XN_03N129W	090419	1.87	22.3	22.0 ± 1.0
B16_015921_3568_XN_03N260W	091219	1.87	20.4	9.1 ± 0.3

the line agrees closely with the predicted position based on the optical design of the CTX. Ultimately, a 5th-order polynomial fit of CCD pixel number versus field angle was derived that allows for the removal of the minor distortion found across the 5.7° CTX field of view for each row of imaging data. The specific form of the polynomial fit is corrected pixel number = $2502 + 872.37\alpha + 0.877239\alpha^3 + 0.030\alpha^5$, where α is the angle (in degrees) from the optical axis (centered on pixel 2502). The maximum amplitude of this correction is approximately 8-10 pixels at the edges of the CTX field of view, or about 50 meters on Mars from the nominal MRO mapping orbit altitude.

CTX in-flight performance and calibration monitoring and validation

During the cruise to Mars and subsequent Mars orbital operations, the performance of CTX has been monitored periodically to assess the nature and magnitude of any changes in the instrument's bias and dark current level, flatfield behavior, radiometric responsivity, and scattered/stray light behavior. As of this writing (early-2013), the instrument has delivered stable and consistent performance.

In-flight bias and dark current monitoring

The CTX detector's background bias and dark current levels are monitored in flight by acquiring dedicated image sequences of the night side of Mars, far from the terminator. For the purposes of this paper, we consider seven such sequences acquired between April 2007 and December 2009 (Table 2). These night side CTX observations have an average signal value of 12.5 ± 5.8 DN and show no systematic variations with time. Similarly, no correlated changes were observed in dark signal levels between odd and even CTX pixels. The average CTX FPA temperature for these dark measurements was 21.1 ± 1.4°C. Based on pre-flight data and Equation 1, the average CTX dark current signal accumulated in a 1.87 msec exposure at 21.1°C is predicted to be 12.2 DN, identical to the observed night-side dark signal levels within the uncertainties.

An assessment of the stability of the CTX bias and dark current performance over the entire ~1500 days of the MRO mission to date can be obtained by plotting the time history of the average values of the masked reference pixels downlinked with each CTX image. Those averages are compared to the average CTX FPA operating temperature history in Fig. 7. The average CTX FPA operating temperature to date is 20.7 ± 1.6°C, and deviations in the instrument's FPA temperature generally correlate in a sinusoidal fashion with Mars heliocentric distance: 2-3°C cooler near aphelion and 2-3° warmer near perihelion (Fig. 7; higher-frequency deviations in instrument temperature are usually related to changes in nominal spacecraft attitude and to the occasional effects of large-scale planet-encircling dust storms). The CTX masked reference pixel average DN values generally correlate with FPA temperature, with an overall average during the mission of 33.6 ± 11.6 DN, or only about 0.8% of the instrument's full dynamic range. Small systematic variations in the CTX bias and dark current level were observed to correlate with changes in spacecraft attitude (and thus temperature) or observing modes/use (e.g., more intensive imaging during times of higher available downlink).

In-flight flatfield monitoring and refinement

During flight operations in Mars orbit, the MRO spacecraft is nominally oriented so that the long axis of the CTX CCD line array is oriented perpendicular to the spacecraft's velocity vector, allowing the array to "pushbroom" across the surface and image long swaths of terrain. Twice during the mission (in Nov. 2006 and July 2007; Table 3), the spacecraft's attitude was rotated by 90° in yaw around the +z axis (the axis pointing towards nadir) so that the long axis of the CTX linear array was oriented parallel to the direction of spacecraft motion. Imaging during that attitude results in a smearing of the terrain across all the CTX pixels. Averaging of large numbers of multiple, continuously terrain-smeared pixels like this can be used to approximate a low-frequency, average "flatfield" data set in flight, in a way similar to the in-flight flatfielding methods of Lucey et al. (1997) and McEwen and Robinson (1997).

The average CTX flatfield array generated from all of the in-flight 90° yaw sequences (Table 3) is very similar to the pre-flight integrating sphere flatfield array (Fig. 5). Maximum deviations are typically within ±1%, verifying the overall stability of the CTX CCD's pixel-to-pixel response variations over the ~3 years between the pre-flight and in-flight tests. Because the differences are small and the in-flight flatfielding methods could be susceptible to minor high-frequency systematic errors related to the specific terrain imaged, the pre-flight flatfield vector remains the default CTX flatfield for the NASA Planetary Data System (PDS) archive.

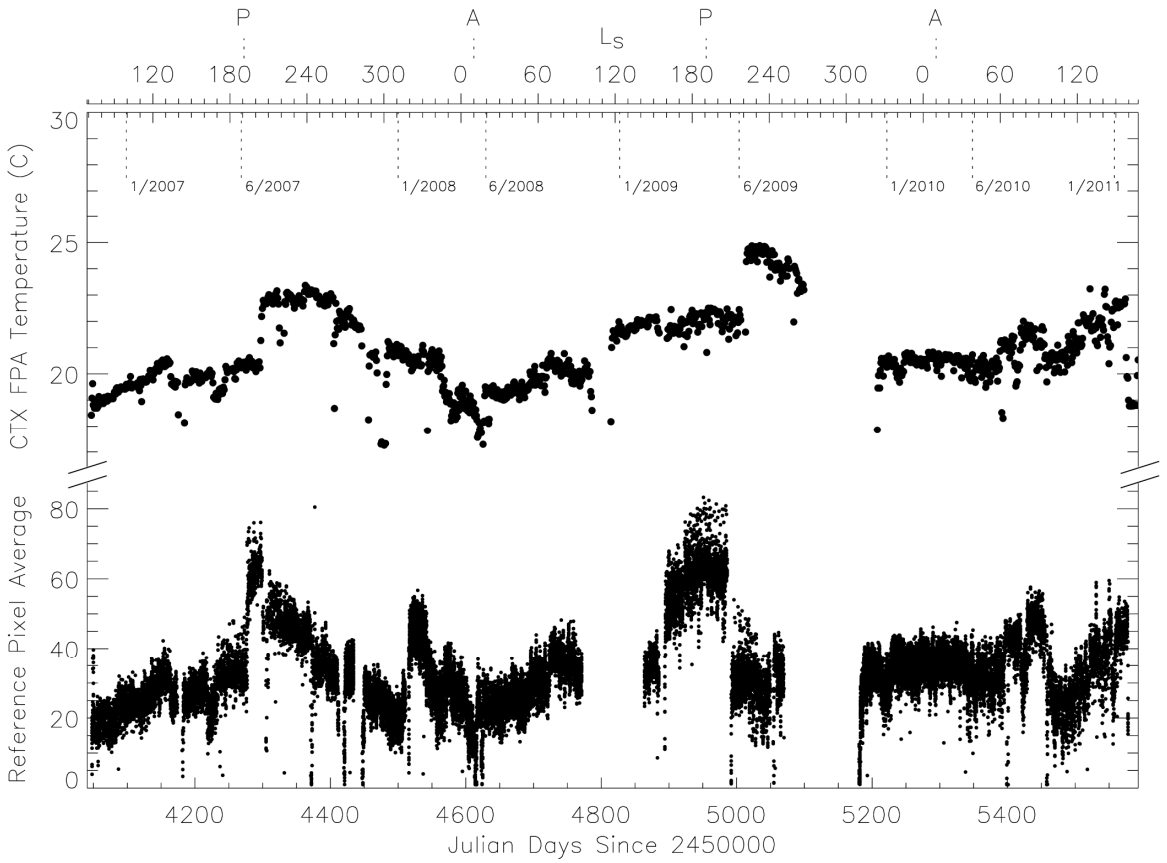

Figure 7. Time history of the CTX Focal Plane Array (FPA) temperature (top data set) and average masked reference pixel value (in DN; bottom data set) during imaging operations over the course of the MRO Primary Science Phase (beginning Nov. 2006) through January 2011 in the Extended Mission. The upper x-axis indicates the areocentric longitude of the Sun (L_s=0° is the start of N. hemisphere spring), and times when Mars was at perihelion ("P") and aphelion ("A") are also indicated. Earth calendar dates at six month intervals are also indicated near the top. The average reference pixel value shows an approximately sinusoidal character that correlates with FPA temperature, which is partly a function of heliocentric distance (Figure07.jpg).

Table 3: In-Flight CTX Flatfield Measurements.

File Name	Date (YYMMDD)	Exp (msec)	FPA Temp (°C)	S/C Attitude
P01_001353_1278_XN_52S133W	061109	1.87	19.3	90° yaw around +z
P01_001353_1377_XN_42S134W	061109	1.87	19.5	90° yaw around +z
P01_001353_1510_XN_29S136W	061109	1.87	19.5	90° yaw around +z
P01_001355_1813_XN_01N195W	061110	1.87	20.1	90° yaw around +z
P01_001355_1985_XN_18N197W	061110	1.87	20.1	90° yaw around +z
P01_001355_2034_XN_23N197W	061110	1.87	20.1	90° yaw around +z
P01_001355_2092_XN_29N198W	061110	1.87	20.1	90° yaw around +z
P01_001355_2233_XN_43N200W	061110	1.87	20.2	90° yaw around +z
P01_001355_2279_XN_47N201W	061110	1.87	20.3	90° yaw around +z
P09_004675_2185_XN_38N109W	070726	1.87	22.5	90° yaw around +z
P09_004675_2233_XN_43N110W	070726	1.87	22.4	90° yaw around +z
P09_004675_2306_XN_50N111W	070726	1.87	22.6	90° yaw around +z
P09_004676_2161_XN_36N136W	070726	1.87	21.6	90° yaw around +z
P09_004676_2228_XN_42N137W	070726	1.87	21.8	90° yaw around +z
P09_004676_2292_XN_49N138W	070726	1.87	21.8	90° yaw around +z

Radiometric Validation

To attempt to validate the radiometric calibration of CTX in flight, we compared the estimated Lambert albedos of CTX images obtained along the traverse paths of the Mars Exploration Rovers (MER) Spirit and Opportunity to estimated Lambert albedos for the same regions derived from images from the Mars Global Surveyor Mars Orbiter Camera (MGS/MOC), the MRO Mars Color Imager (MARCI), and the MER Panoramic Cameras (Pancams) on the rovers themselves. Details below show that the overall comparison is very favorable, validating the CTX radiometric calibration within the uncertainties of the radiometric accuracies of these various investigations and the assumption of Lambertian behavior of the Martian surface.

Estimating CTX Lambert albedo along the MER traverses. We identified, calibrated, and map-projected two CTX images along the MER traverse paths (Fig. 8) using pre-flight calibration files and the radiometric coefficient described above. The mapping routines are analogous to those developed for MGS/MOC images (Malin et al. 1992; Malin et al. 2007). Image P01_001414_1780_XI_02S005W (acquired Nov. 14, 2006 at emission angle e = 10°, incidence angle i = 54°, and phase angle g = 44°) covers Opportunity's traverse through a relatively low albedo region in Meridiani Planum. For Spirit's traverse through a relatively high albedo region in Gusev crater, we employed image P05_003122_1653_XI_14S184W (acquired March 27, 2007 at e = 4°, i = 54°, and g = 50°). Both images were acquired during relatively low atmospheric dust opacity conditions (τ = 0.48 and 0.62, respectively; Lemmon et al. 2004). These CTX images were calibrated to radiance (I, in W/m^2/μm/sr) and then divided by the solar irradiance at the top of the Martian atmosphere at the time of the observation (J = πF, in W/m^2/μm, where F = solar spectral radiance in W/m^2/μm/sr from Wehrli, 1986) to generate the so-called radiance factor (I/F), a parameter that is comparable to reflectance (Hapke, 1993). Dividing I/F by the cosine of the average incidence angle of the scene yields an estimate of the Lambert albedo (Hapke, 1993), assuming that the surface is indeed Lambertian at least at these phase angles (a generally reasonable approximation; see, e.g., Soderblom et al. 2006).

Comparison of Pancam, MOC, and CTX estimated Lambert albedos. For comparisons with Pancam and MOC derived average estimated Lambert albedo values, we averaged CTX-based estimated Lambert albedo values within circular regions of radius 85 m along each rover traverse,. The albedos estimated from CTX images along the rovers' traverse paths are plotted vs. distance along the traverses in Fig. 9, where they are also compared with the Lambert albedos estimated by Bell et al. (2008) from Pancam and MOC images along the traverses. The gray stippled region surrounding the estimated CTX Lambert albedos in Fig. 9 represents a ±10% variation.

The estimated Lambert albedos from CTX along the two traverses follow the general trends of the Pancam and MOC estimated Lambert albedos for the same regions. However, MOC and Pancam Lambert albedo estimates are systematically about 10-20% higher than CTX values. This discrepancy can be understood by a comparison of the CTX, MOC, and Pancam passbands (Fig. 10), which shows that CTX samples a narrower and shorter-wavelength segment (λeff ~ 611 nm; Fig. 6) of Martian reflected sunlight than MOC (λeff ~ 700 nm; Malin et al. 1992) or the Pancam "empty" (L1: 739 nm; Bell et al. 2003) filters. The quantitative difference in radiance factor that would be observed by each instrument [$(I/F)_{inst}$] observing an average

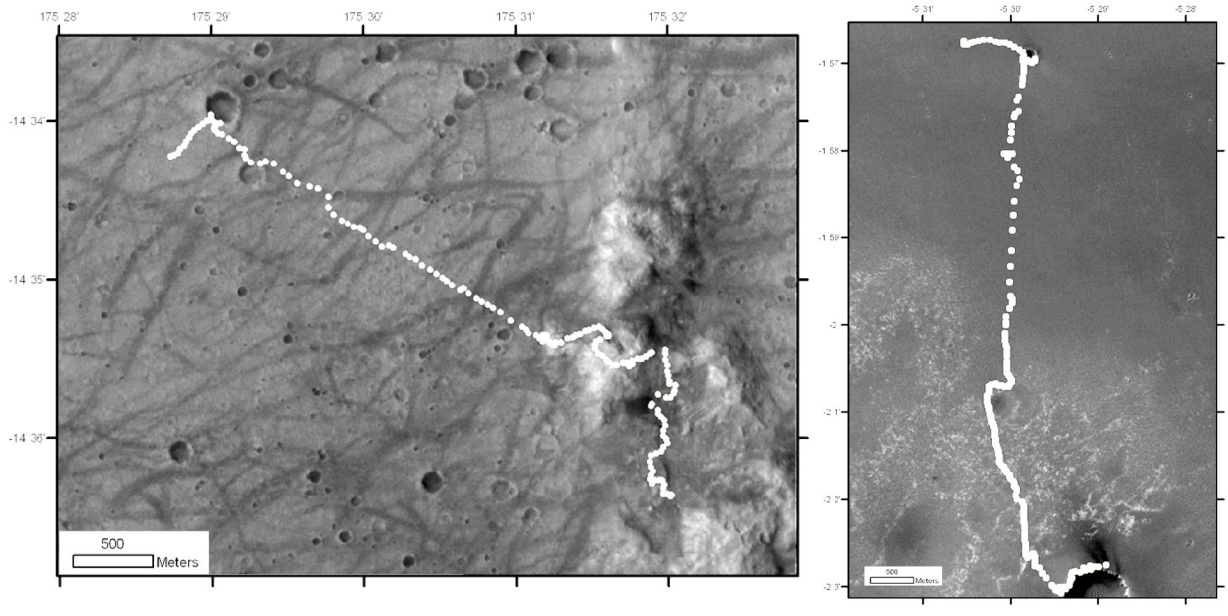

Figure 8. (Left) Traverse path for the Mars Exploration Rover Spirit (white points) overlaid on a portion of CTX image P05_003122_1653_XI_14S184W. (Right) Traverse path for the Opportunity rover overlaid on a portion of CTX image P01_001414_1780_XI_02S005W (Figure08.jpg).

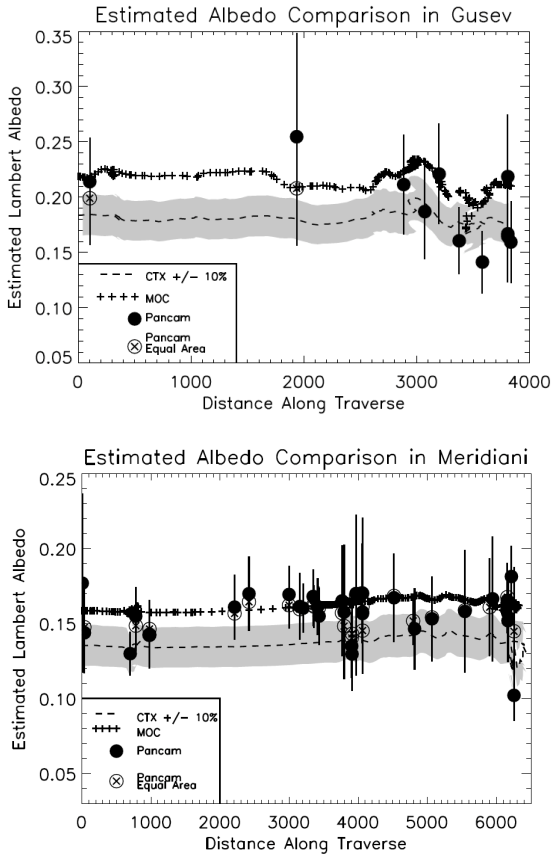

Figure 9. Estimated Lambert albedo values measured by Pancam (solid circles; circles with an X are equal area averages), MOC (crosses) and CTX (dashes) at Gusev (top) and Meridiani Planum (bottom), plotted against traverse distance. The uncertainties for the Pancam measurements correspond to the albedo variance within the selected scene, not to instrumental errors. An equal-area averaging of the Pancam albedos has been applied to the scenes with little or no topography (⊗). Estimated uncertainties on the MOC-derived albedos are ±10-20%; representative ±10% uncertainties on the CTX-derived albedos are indicated by the gray shading (Figure09.jpg).

Mars bright region can be estimated as:

$$(I/F)_{Inst} = \frac{\int J_{Sun} R_{Mars} T_{Inst} d\lambda}{\int J_{Sun} R_{Mars} d\lambda} \qquad (2),$$

where J_{Sun} is the solar spectral irradiance at Mars (e.g., Wehrli, 1986), R_{Mars} is an average Martian bright region reflectance spectrum (e.g., Mustard and Bell, 1994), T_{Inst} is the normalized spectral transmission profile of each instrument (e.g., Malin et al. 1992; Malin et al. 2007), and the integral is taken over the full solar spectral reflectance wavelength interval (~200 to 3000 nm). The denominator of Equation 2 is the CTX band-integrated solar irradiance (J_{CTX}), which at 1 AU is 1671.7 W/m^2/μm. Figure 10 shows a graphical example of this comparison for CTX, MOC, and Pancam, all hypothetically observing the same average

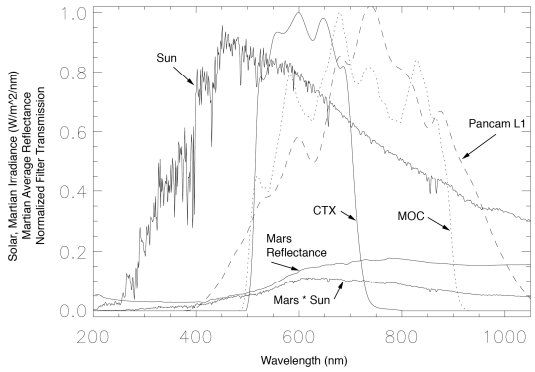

Figure 10. Comparison of the CTX, MOC, and Pancam "empty" (Filter L1; Bell et al., 2003) instrument filter transmission bandpasses (normalized to 1.0 at their respective peaks) to the solar spectral irradiance (Wehrli, 1986) and the reflected irradiance that would be observed from a region with an average Mars reflectance spectrum (e.g., Mustard & Bell, 1994) (Figure10.jpg).

Martian bright region. Performing this comparison reveals that the ratio of $(I/F)_{MOC}$ to $(I/F)_{Pancam}$ should be ~ 1.0, but that the ratio of $(I/F)_{MOC}$ to $(I/F)_{CTX}$ or $(I/F)_{Pancam}$ to $(I/F)_{CTX}$ should be ~ 1.15 for the same region observed under the same conditions. This is not surprising, given the fact that the CTX bandpass samples more of the lower reflectance near-UV reflectance drop-off ("red edge") of the Martian spectrum, and thus less reflected radiance for the same region, than MOC or Pancam's L1 filter.

Thus, while there is still some uncertainty in this comparison, the discrepancy in estimated Lambert albedo values between MOC (and Pancam) and CTX appears to be mostly related to the differences in effective bandpasses of the instruments. For images of average Mars regions acquired at similar incidence angles, CTX albedo estimates would be around 15% lower than those estimated by MOC and Pancam, as well as estimated bolometric albedos from the Viking IRTM (Chase et al. 1978) and MGS/TES (Christensen et al. 2001) instruments. In general, however, the correction factor needed to compare CTX-estimated albedos with those derived from other instruments would also need to take into account potentially differences in viewing geometry, as well as non-trivial variations in atmospheric dust opacity between the observations. Given all of the potential sources of errors and uncertainties, it is actually quite remarkable that CTX, MOC, and Pancam estimated Lambert albedos agree to within 10-20% over the rover traverse areas. This result would appear to validate the absolute calibration of all of these instruments, within the levels of their respective uncertainties.

Comparison of MARCI and CTX estimated Lambert albedos. We also performed a comparison of estimated Lambert albedos between CTX and the MRO Mars Color Imager (MARCI) ~1 km/pixel resolution data over the rover traverse paths in Fig. 8. Calibrated, low atmospheric dust opacity 5-

Table 4. In-Flight CTX Stray/Scattered Light Test Measurements.

File Name	Date (YYMMDD)	Exp (msec)	FPA Temp (°C)	Observation
P02_001762_2348_XN_54N145W	061211	1.87	19.0	view of bright crater wall at 30° pitch angle
P02_001762_2481_XN_99N999W	061211	1.87	19.1	scan past northern limb
P02_001762_2740_XN_99N999W	061211	19.99	19.2	scan at max angle above the northern limb
P12_005558_0858_XN_85S305W	071003	22.99	22.0	scan past southern limb

color MARCI radiances (Bell et al. 2009) were averaged from ~10 pixels from image P01_001414_1353_MA_00N004W over the Opportunity site and from ~20 pixels from image P05_003122_2081_MA_00N186W over the Spirit site. MARCI radiances spanning effective wavelengths from 437 to 718 nm were resampled with minor extrapolation to span the ~400 to 800 nm wavelength range of CTX (Fig. 6) and then integrated over the CTX bandpass to make a "broadband MARCI" estimate of the radiance (IMARCI) over each traverse. The broadband MARCI Lambert albedo (AMARCI) can then be estimated as:

$$A_{MARCI} = \left\{(I_{MARCI})/\left[(J_{CTX}/\pi)\right]/D^2\right\}/\cos(i_{MARCI}) \quad (3)$$

where J_{CTX} = 1671.7 W/m^2/μm at 1 AU; D = the heliocentric distance of Mars for each MARCI image, and i_{MARCI} = the average solar incidence angle. Employing the values of I_{MARCI} = 31.7 and 17.9 W/m^2/μm/sr, D = 1.4145 and 1.5750 AU, and i_{MARCI} = 54.3° and 54.3°, over the Spirit and Opportunity traverses respectively, yields an estimated MARCI-based Lambert albedo over the Spirit site of 0.204 and over the Opportunity site of 0.143. Uncertainties in the MARCI-based albedo estimates are of order ±10-20% based on the observed dispersion of MARCI radiances along the traverse paths in Fig. 8. These values are remarkably close to the average estimated CTX Lambert albedos for the sites shown in Fig. 9. Thus, it would appear that this analysis provides another independent validation of the CTX radiometric calibration reported above.

In-flight Scattered and stray light assessment

Pre-flight CTX testing revealed extremely low levels of internal stray/scattered light in the instrument. A few opportunities were identified in flight to verify this excellent stray light rejection performance (Table 4). Imaging of a bright crater wall near 54°N, 145°W did not reveal any measureable scattered light in adjacent dark terrains, and imaging at maximum range from the limb showed only 1-2 DN of signal above the space background. The December 2006 CTX scan across the northern limb did not prove to be useful (from a scattered light perspective) due to the presence of significant high-altitude dust and detached limb hazes, which effectively make the analysis of potential stray or scattered light across the fuzzy limb/space boundary intractable.

The October 2007 CTX image P12_005558_0858_XN_85S305W, which scanned across the southern limb, was more useful for scattered/stray light analysis because the limb/space boundary was much sharper (Fig. 11). Analysis of light levels off the limb in the direction perpendicular to the CTX line array detector (Line 1 in Fig. 11) shows that off-axis scattered light falls to less than 1% of the on-axis signal within 0.1° of the limb (the peak expected on-planet signal for these observations was assumed to be ~43,000 DN, which is the typical signal level for bright south polar terrains (~3500 DN) multiplied by the ratio of the actual vs. average exposure time of this limb scan sequence: 22.99/1.87 msec).

Stray light within the instrument is more difficult to characterize. Analysis of light levels off of the limb in the direction parallel to the CTX line array shows that when the array is half or more illuminated (Line 2 in Fig. 11), stray

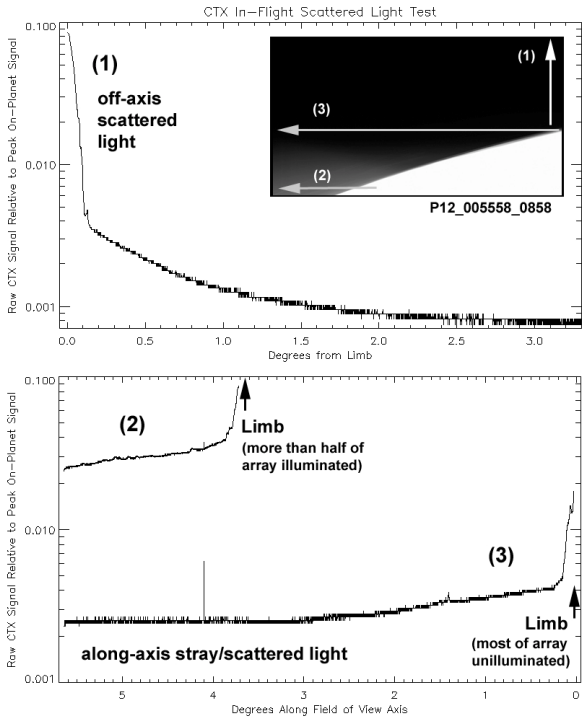

Figure 11. Example of scattered/stray light behavior in 3 Oct. 2007 CTX limb scan image P12_005558_0858_XN_85S305W (inset). Line 1 (top plot) shows the sharp fall-off in scattered light in the direction perpendicular to the CTX line array. Line 2 (bottom plot) shows evidence of some internal stray light at the 3-5% level, but some of that signal may be related to diffuse or detached (spikes in the data) dust/cloud hazes in this area just above the mid-summer south polar cap. Line 3, like Line 1, shows a much sharper drop-off in signal level when little or none of the CTX array is actually illuminated (Figure11.jpg)

light levels appear to be ~ 3-5% of the on-axis signal level. However, the presence of diffuse and detached dust/cloud hazes near the limb complicate this assessment. That is to say, some of that "stray light" may actually be produced by Mars itself (i.e., high altitude atmospheric scattering). When the source was at the edge of the array (Line 3 in Fig. 11), stray light levels fall very quickly to less than 1% of the on-axis signal within 0.1° of the limb.

While not perfect tests, these observations reveal that stray/scattered light levels in the CTX data are very low, and are not likely to represent significant sources of contaminating radiance.

CTX calibration pipeline

Raw CTX images

Raw CTX Experiment Data Records (EDRs) can be obtained from the NASA Planetary Data System (PDS, e.g., http://pds-imaging.jpl.nasa.gov/Admin/resources/cd_mro.html). The images have been depacketized, decompressed, and reformatted with a standard PDS text label that identifies various properties of the image and the observation circumstances, including information on the byte offset to the data portion of the image, which is appended after the label. CTX images are always a multiple of 16 pixels in both width and height. More detailed documentation on the structure and content of the raw CTX EDRs can also be found online from the PDS in the CTX Software Interface Specifications document (Caplinger, 2007), which is stored within the "document" subdirectories associated with each data volume release (e.g., http://pds-imaging.jpl.nasa.gov/data/mro/mars_reconnaissance_orbiter/ctx/mrox_0023/document/ctxsis.pdf). Details on the file-naming scheme for the PDS-archived raw CTX images is provided in Appendix A.

Calibration algorithm

A straightforward set of calculations and image manipulations can be used to convert raw CTX images into radiometrically-calibrated data.

Decompanding. All CTX data are "companded" (a word originating from "compressed, then later expanded") within the instrument electronics from their original 12-bit (0-4095 DN) format to 8-bit (0-255 DN) data files using a square-root-like compression lookup table (LUT) developed by the CTX team using the CCD gain, read noise, and full well derived during pre-flight camera testing. This onboard compression process is designed to prevent shot noise from being encoded into the downlinked data. The CTX 12-to-8 bit LUT and the 8-to-12 bit inverse LUT needed to "decompand" the original data are summarized in Table 5. That information is also available with each CTX PDS data volume release as a simple ASCII text file called ctxdec.txt that is stored within the "calib" subdirectory. To decompand the raw data, each occurrence of the raw 8-bit value in Table 5 must be replaced with its corresponding 12-bit value. The values in Table 5 are provided digitally in the Supporting Data files associated with this paper.

Bias and Dark Current Subtraction. Both bias and dark current signal accumulate simultaneously during each CTX exposure. While small, the levels can still differ slightly between the A and B channels of the CCD array. A simple process for subtracting this background signal level is to separately calculate the average DN values in the odd (channel A) and even (channel B) masked-off reference pixels (pixels 1-38 and 5039-5056), and then subtract those average values from the corresponding odd and even unmasked pixels (pixels 39-5038).

Flatfielding. The default CTX normalized flatfield calibration file, created using the procedure described above (Fig. 5), is a 5064-element vector named ctxflat.txt available in the "calib" subdirectory of each online CTX PDS data release directory. The flatfield correction is achieved by dividing the bias and dark current-subtracted data by this vector. Other versions of the CTX flatfield array, like the in-flight flatfield discussed above, could potentially give improved performance for some applications (such as mosaicking for geologic, as opposed to radiometric, studies). The alignment of a flatfield vector with the columns of the CTX data can be verified using the ~10% lower "spike" near the middle of the array in the flatfield data of Fig. 5, which occurs at CTX pixel number 2595. This signal drop-off can usually be seen in the raw CTX data and can provide a benchmark to assess the performance of the flatfield correction.

Even/Odd striping correction. Additional cosmetic improvement of CTX images may be obtained by applying another small correction that attempts to specifically remove any systematic detector gain effects that might exist between the A channels and the B channels of the CTX detector. Such even/odd channel gain differences can result in subtle "striping" in calibrated CTX images, even after performing the bias/dark and flatfield calculations discussed above. A simple way to remove any such small residual differences is to calculate, using bias/dark subtracted and flatfielded images, the small difference D between the average of the even column DN values minus the average of the odd column DN values, and then subtract D/2 from the even column data and add D/2 to the odd column data.

Conversion to Radiance and I/F. Decompanded, bias/dark subtracted, and flat-fielded CTX data can be converted to radiance and radiance factor (*I/F*, where *I* is the observed radiance on sensor in W/m^2/μm/sr, and $J = \pi F$ is the solar spectral irradiance at the top of the Martian atmosphere at the time of the observation, in W/m^2/μm; e.g., Hapke, 1993) using the following equations:

$$I = \frac{DN / t_{\exp}}{R} \quad (4),$$

where *DN* is the decompanded, bias/dark subtracted, flat-fielded, and possibly de-striped CTX DN value for each pixel after application of the CTX calibration pipeline

Table 5. CTX 8-bit to 12-bit Companding-Decompanding Table.

8-bit	12-bit	8-bit	12-bit	8-bit	12-bit	8-bit	12-bit	8-bit	12-bit	8-bit	12-bit
0	1	46	179	92	601	138	1269	184	2184	230	3345
1	3	47	186	93	613	139	1286	185	2206	231	3373
2	5	48	193	94	625	140	1304	186	2229	232	3401
3	7	49	199	95	637	141	1321	187	2252	233	3430
4	9	50	206	96	649	142	1339	188	2275	234	3458
5	11	51	213	97	662	143	1356	189	2298	235	3486
6	13	52	220	98	674	144	1374	190	2321	236	3515
7	15	53	228	99	687	145	1392	191	2345	237	3544
8	17	54	235	100	699	146	1410	192	2368	238	3573
9	20	55	243	101	712	147	1429	193	2392	239	3601
10	22	56	250	102	725	148	1447	194	2415	240	3630
11	24	57	258	103	738	149	1465	195	2439	241	3660
12	27	58	266	104	751	150	1484	196	2463	242	3689
13	29	59	274	105	765	151	1502	197	2487	243	3718
14	32	60	282	106	778	152	1521	198	2511	244	3748
15	35	61	290	107	792	153	1540	199	2535	245	3777
16	38	62	298	108	805	154	1559	200	2560	246	3807
17	41	63	306	109	819	155	1578	201	2584	247	3837
18	44	64	315	110	833	156	1598	202	2609	248	3867
19	47	65	324	111	847	157	1617	203	2634	249	3897
20	50	66	332	112	861	158	1636	204	2658	250	3927
21	54	67	341	113	875	159	1656	205	2683	251	3958
22	58	68	350	114	890	160	1676	206	2709	252	3988
23	61	69	359	115	904	161	1696	207	2734	253	4019
24	65	70	369	116	919	162	1715	208	2759	254	4049
25	69	71	378	117	933	163	1736	209	2784	255	4080
26	73	72	387	118	948	164	1756	210	2810		
27	77	73	397	119	963	165	1776	211	2836		
28	82	74	407	120	978	166	1796	212	2861		
29	86	75	416	121	993	167	1817	213	2887		
30	91	76	426	122	1009	168	1838	214	2913		
31	95	77	436	123	1024	169	1858	215	2939		
32	100	78	446	124	1039	170	1879	216	2966		
33	105	79	457	125	1055	171	1900	217	2992		
34	110	80	467	126	1071	172	1921	218	3019		
35	115	81	478	127	1087	173	1943	219	3045		
36	121	82	488	128	1103	174	1964	220	3072		
37	126	83	499	129	1119	175	1985	221	3099		
38	131	84	510	130	1135	176	2007	222	3126		
39	137	85	521	131	1151	177	2029	223	3153		
40	143	86	532	132	1168	178	2050	224	3180		
41	149	87	543	133	1184	179	2072	225	3207		
42	155	88	554	134	1201	180	2094	226	3235		
43	161	89	566	135	1218	181	2117	227	3262		
44	167	90	577	136	1235	182	2139	228	3290		
45	173	91	589	137	1252	183	2161	229	3317		

calculations; t_{exp} is the exposure time of the image in milliseconds, and R is the CTX responsivity coefficient [13.1 (DN/msec)/(W/m^2/μm/sr)] described in Section 2.5.

To convert the derived CTX radiance (I) to radiance factor (I/F) requires an estimate of F, the solar radiance at the top of the Martian atmosphere at the time of the observation. F can be estimated by:

$$F = (J_{CTX} / \pi) / D^2 \quad (5),$$

where J_{CTX} is the solar spectral irradiance at 1 AU (Wehrli, 1986) convolved with the CTX bandpass profile (1671.7 Watts/m^2/μm) and D is the heliocentric distance of Mars at the time of each CTX observation, in AU. I/F can be further converted into an estimated Lambert albedo through division by the cosine of the solar incidence angle for each pixel. As described in the literature (e.g., McConnochie et al. 2006; Bell et al. 1999; Bell et al. 2006; Bell et al. 2008; Bell et al. 2009), it is important to remember that this approach would result in only an estimate of the Lambert albedo over a particular bandpass (specifically, 611±189 nm; see Fig. 6). As such, it is not directly comparable to broadband albedos such as those derived from MGS/TES or Viking IRTM, without additional analysis.

More generally, additional details of the CTX calibration pipeline process are described within the file called ctxcal.txt that is stored online within the "calib" subdirectory associated with each CTX PDS data volume release, and for users of the USGS ISIS 3 image processing software, within the documentation for the "ctxcal" and "ctxoddeven" functions.

Summary

The MRO/CTX instrument was designed to acquire high resolution monochromatic images in order to enable a variety of detailed investigations of geologic processes on

Mars. The instrument is based on a single 5056-element CCD line array with 5000 unmasked, active elements. From the beginning of the MRO Primary Science Phase in November 2006 through April, 2013, pushbrooming of the array along the direction of spacecraft motion has enabled nearly 82% of the Martian surface to be imaged at ~6 m/pixel resolution. Pre-flight and in-flight calibration of the instrument provide the ability to create cosmetically appealing image strips ~30 km wide, and to measure the radiance on sensor (in, for example, $W/m^2/\mu m/sr$), radiance factor (I/F), or Lambert albedo of imaged regions to an estimated absolute uncertainty of ~10-20%.

Calibration and manipulation of CTX images is relatively straightforward. Processing steps include decompanding the raw data from 8- to 12-bit format, subtracting any background bias/dark current signal, correcting for pixel-to-pixel non-uniformity (flatfield) variations, and scaling to radiance or radiance factor based on pre-flight laboratory calibrations.

The CTX investigation is acquiring the highest spatial resolution imaging coverage yet obtained over such a large fraction of the Martian surface. As such, this data set represents an enormously valuable resource for planetary scientists. CTX images provide critical local context for higher-resolution MRO/High Resolution Imaging Science Experiment (HiRISE) (McEwen et al. 2007) images at 0.3 to 0.5 m/pix and MGS/MOC (Malin et al. 1992) images at 1.5 m/pix, both of which only cover a few percent of the Martian surface. In addition, CTX images and CTX regional mosaics provide important geologic context for lower spatial resolution multispectral and hyperspectral investigations like MGS/TES, Mars Odyssey/Thermal Emission Imaging System (THEMIS) (Christensen et al. 2004), Mars Express/ OMEGA (Bibring et al. 2004), and MRO/Compact Reconnaissance Imaging Spectrometer for Mars (CRISM) Murchie et al. 2007). CTX continues to operate well from Mars orbit, and there is every expectation that as the percentage of the surface covered continues to increase, the discoveries enabled by the CTX investigation will also continue.

Appendix A: CTX File Naming Scheme

The naming convention for CTX images archived in the NASA Planetary Data System is as follows:

ppp_nnnnnn_tttt_xx_aahbbbW.IMG

where:

ppp = Mission phase descriptor, which is one of:

CRU: Cruise check-out/calibration (Aug.-Dec. 2005);

MOI: post-Mars Orbit Insertion check-out (Mar. 2006);

T01: Transition to Primary Mission (Sep.-Oct. 2006);

P*cc*: Primary Mission (Nov. 2006 - Aug. 2008),

(in which *cc* is an integer from 01 to 23);

B*cc*: Primary & Extended Mission (Sep. 2008-Jun. 2010),

(in which *cc* is an integer from 01 to 22);

G*cc*: Extended Mission (July 2010 through May 2012),

(in which *cc* is an integer from 01 to 23);

D*cc*: Extended Mission (next Mars year past June 2012)

nnnnnn = Mars orbit number (if after MOI).

tttt = center latitude of image relative to the descending equator crossing on the dark side of the planet (tttt = 0000), where the last digit is the first decimal place to nearest 0.1 degree. For example, the south pole = "0900", dayside equator = "1800", north pole = "2700".

xx = "XI" or "XN", where "X" stands for CTX, I = ITL (Integrated Target List) commanded images, and N = NIFL (Non-Interactive File Load) commanded images.

aa = center latitude of planned image, to nearest degree.

h = hemisphere, "N" or "S".

bbb = center longitude of planned image, to nearest degree.

W = the letter "W", denoting positive west longitude.

Note that the mission phase descriptor naming scheme was developed to be consistent with that of the Mars Global Surveyor (MGS) Mars Orbiter Camera (MOC) dataset to simplify comparisons of data across several Mars years. The areocentric solar longitude (L_s) range of a given numbered Earth month is roughly the same across the two datasets; for example, MGS MOC periods M12, E12, R12, and S12 correspond to MRO CTX periods P12, B12, and G12. Use of the letter B represents beta, the second Mars year of CTX imaging; G represents gamma, the third Mars year; the next letter is D, delta, the fourth Mars year, etc.

Note also that CTX planning periods for Primary Mission and beyond are defined by Mars year and Earth month; the letter represents Mars year, and the number represents Earth month within that Mars year.

Acknowledgements

The CTX development, operations, and science teams are privileged to have had an enormous amount of help with this investigation from the Mars Reconnaissance Orbiter spacecraft and operations teams at Lockheed Martin (Denver, CO) and the Jet Propulsion Laboratory (Pasadena, CA). The authors also thank Ryan Anderson, Derek Schaeffer, and Karrie Kressler for assistance with CTX calibration and mapping software. We thank Ron Li and colleagues at Ohio State Univ. for assistance identifying the Spirit and Opportunity traverse coordinates in Fig. 8. This work was funded by NASA contracts from the MRO Project to Malin Space Science Systems, Inc., Cornell University, and Arizona State University.

References

Bell III, J.F., M.J. Wolff, T.C. Daley, D. Crisp, P.B. James, S.W. Lee, J.T. Trauger, and R.W. Evans (1999) Near-infrared imaging of Mars from HST: Surface reflectance, photometric properties, and implications for MOLA data, *Icarus, 138,* 25-35. doi:10.1006/icar.1998.6057.

Bell III, J.F. et al. (2003) The Mars Exploration Rover Athena Panoramic Camera (Pancam) Investigation, J. Geophys. Res., 108, E12. doi:10.1029/2003JE002070.

Bell III, J.F., J. Joseph, J.N. Sohl-Dickstein, H.M. Arneson, M.J. Johnson, M.T. Lemmon, and D. Savransky (2006) In-flight calibration and performance of the Mars Exploration Rover Panoramic Camera (Pancam) Instruments, *J. Geophys. Res., 111,* E02S03. doi:10.1029/2005JE002444.

Bell III, J.F., M.S. Rice, J.R. Johnson, and T.M. Hare (2008) Surface albedo observations at Gusev Crater and Meridiani Planum, Mars, J. Geophys. Res., 113, E06S18. doi:10.1029/2007JE002976.

Bell III, J.F. et al. (2009) Mars Reconnaissance Orbiter Mars Color Imager (MARCI): Instrument description, calibration, and performance, J. Geophys. Res., 114, E08S92. doi:10.1029/2008JE003315.

Bibring, J.-P. et al. (2004) OMEGA: Observatoire pour la Minéralogie, l'Eau, les Glaces et l'Activité, In: Mars Express: The Scientific Payload. A. Wilson and A. Chicarro, eds. ESA SP-1240, Noordwijk, Netherlands: ESA Publications Division, pp. 37–49. http://sci.esa.int/science-e/www/object/doc.cfm?fobjectid=34883.

Caplinger, M. (2007) Mars Reconnaissance Orbiter Software Interface Specification, Mars Color Imager (MARCI) Standard Product, Malin Space Science Systems, Inc. http://pds-imaging.jpl.nasa.gov/data/mro/mars_reconnaissance_orbiter/marci/mrom_0001/document/marcisis.pdf.

Chase, Jr., S.C. et al. (1978) Viking Infrared Thermal Mapper, Appl. Opt., 17, 1243-1251.

Christensen, P. R. et al. (2001) The Mars Global Surveyor Thermal Emission Spectrometer experiment: investigation description and surface science results. J. Geophys. Res. 106, 23,823–23,871. 10.1029/2000JE001370.

Christensen, P. R. et al. (2004) Thermal Emission Imaging System (THEMIS) for the Mars 2001 Odyssey Mission, Space Science Reviews, 110, 85–130. 10.1023/B:SPAC.0000021008.16305.94

Hapke B. (1993) Theory of Reflectance and Emittance Spectroscopy, Cambridge Univ. Press, New York, 455 pp.

Janesick, J.R., K.P. Klaasen, and T. Elliot (1987) Charge-coupled device charge-collection efficiency and the photon transfer technique, Opt. Eng., 26, 972-980.

Lemmon, M. et al. (2004) Atmospheric Imaging Results from the Mars Exploration Rovers: Spirit and Opportunity, *Science*, *306*, 1753-1756. doi:10.1126/science.1104474.

Lucey, P. G., J. L. Hinrichs, M. S. Robinson, J. Johnson, C. A. Peterson, N. Domergue-Schmidt, and G. J. Taylor (1997), Near-infrared (1.0–2.0 microns) global imaging of the moon, Lunar Planet. Sci., XXVIII, Abstract 1398.

Malin, M.C., G.E. Danielson, A.P. Ingersoll, H. Masursky, J. Veverka, M.A. Ravine, and T.A. Soulanille (1992) Mars Observer Camera, J. Geophys. Res., 97, 7699–7718.

Malin, M.C., et al. (2007) Context Camera investigation on board the Mars Reconnaissance Orbiter, J. Geophys. Res., 112, E05S04. doi:10.1029/2006JE002808.

Mars Reconnaissance Orbiter (2005) MRO Mars Color Imager (MARCI) and Context Camera (CTX) Pre-Flight Calibration Report, MSSS-CTX-DOC-2002, Malin Space Science Systems, Inc.

McConnochie, T.H., J.F. Bell III, D. Savransky, G. Mehall, M. Caplinger, P. R. Christensen, L. Cherednik, K. Bender, A. Dombovari (2006) Calibration and In-Flight Performance of the Mars Odyssey THEMIS Visible Imaging Subsystem (VIS) Instrument, *J. Geophys. Res., 111,* E06018. doi:10.1029/2005JE002568.

McEwen, A.S. and M.S. Robinson (1997), Mapping of the Moon by Clementine, Adv. Space Res., 19, 1523 – 1533, doi:10.1016/S0273-1177(97)00365-7.

McEwen, A.S. et al. (2007) Mars Reconnaissance Orbiter's High Resolution Imaging Science Experiment (HiRISE), J. Geophys. Res., 112, CiteID E05S02. doi:10.1029/2005JE002605.

Murchie, S. et al. (2007) Compact Reconnaissance Imaging Spectrometer for Mars (CRISM) on Mars Reconnaissance Orbiter (MRO), J. Geophys. Res., 112, CiteID E05S03. doi:10.1029/2006JE002682.

Mustard, J.F. and J.F. Bell III (1994) New composite reflectance spectra of Mars from 0.4 to 3.14 μm, Geophys. Res. Lett., 21, 353-356. doi:10.1029/94GL00198.

Soderblom, J.M., J.F. Bell III, M.Y.H. Hubbard, and M.J. Wolff (2006) Martian phase function: Modeling the visible to near-infrared surface photometric function using HST-WFPC2 data, Icarus, 184, 401-423. doi:10.1016/j.icarus.2006.05.006.

Wehrli, C. (1986) Solar Spectral Irradiance, World Climate Research Programme, Pub. Series No. 7, WMO ITD-No. 149, pp 119-126, World Radiation Center, Davos-Dorf, Switzerland.

Zurek, R.W. and S.E. Smrekar (2007) An overview of the Mars Reconnaissance Orbiter (MRO) science mission, J. Geophys. Res., 112, E05S01. doi:10.1029/2006JE002701.

Directory of Supporting Data

Root Directory

Bell_CTX_Cal_MarsJournal_submitted.pdf

Fig. 1	Figure01.jpg
Fig. 2	Figure02.jpg
Fig. 3	Figure03.jpg
Fig. 4	Figure04.jpg
Fig. 5	Figure05.jpg
	PDS_ctxflat.txt
Fig. 6	Figure06.jpg
	ctx-dat_norm.txt
Fig. 7	Figure07.jpg
Fig. 8	Figure08.jpg
Fig. 9	Figure09.jpg
Fig. 10	Figure10.jpg
Fig. 11	Figure11.jpg
Table 5	ctx_companding.txt